Nanoscale

RSC Publishing

PAPER

View Article Online
View Journal | View Issue

Nitrogen doped holey graphene as an efficient metal-free multifunctional electrochemical catalyst for hydrazine oxidation and oxygen reduction†

Cite this: *Nanoscale*, 2013, **5**, 3457

Dingshan Yu,[a] Li Wei,[a] Wenchao Jiang,[a] Hong Wang,[a] Bo Sun,[b] Qiang Zhang,[c] Kunli Goh,[a] Rongmei Si[a] and Yuan Chen*[a]

Electrocatalysts for anode or cathode reactions are at the heart of electrochemical energy conversion and storage devices. Molecular design of carbon based nanomaterials may create the next generation electrochemical catalysts for broad applications. Herein, we present the synthesis of a three-dimensional (3D) nanostructure with a large surface area (784 $m^2 g^{-1}$) composed of nitrogen doped (up to 8.6 at.%) holey graphene. The holey structure of graphene sheets (~25% of surface area is attributed to pores) engenders more exposed catalytic active edge sites. Nitrogen doping further improves catalytic activity, while the formation of the 3D porous nanostructure significantly reduces graphene nanosheet stacking and facilitates the diffusion of reactants/electrolytes. The three factors work together, leading to superb electrochemical catalytic activities for both hydrazine oxidation (its current generation ability is comparable to that of 10 wt% Pt–C catalyst) and oxygen reduction (its limiting current is comparable to that of 20 wt% Pt–C catalyst) with four-electron transfer processes and excellent durability.

Received 24th December 2012
Accepted 15th February 2013

DOI: 10.1039/c3nr34267k

www.rsc.org/nanoscale

Introduction

Increasing energy demands have spurred intense research on electrochemical energy conversion and storage devices, such as fuel cells and metal–air batteries. Electrocatalysts for anode or cathode reactions are at the heart of these devices.[1,2] Noble metals, such as Pt and Pd, have excellent electrocatalytic activity,[3,4] however, their prohibitive cost and weak durability hamper their applications. Therefore, the design and synthesis of alternative electrocatalysts with excellent catalytic performance and enhanced stability and reduced cost is highly desirable but remains challenging.[5–15] Because of their unique structural, physical, and chemical properties,[16–19] nanocarbon materials, particularly nitrogen-doped nanocarbons, have been exploited as potential electrocatalysts in various electrochemical energy conversions, such as oxygen reduction reaction (ORR), NO oxidation, and hydrogen production.[9–15,20–23] Among different nanocarbon materials, two-dimensional (2D) graphene is promising as a feasible electrocatalyst[24–26] because of its high surface area, excellent electrical conductivity, unique graphitized basal plane structure, and low-cost.[27–31] Like many other graphitic materials,[9,32,33] the graphitic edge sites of graphene possess higher reactivity compared to its flat basal plane.[33–35] However, graphene has a relatively low-density of edge sites relative to its abundant basal plane sites.[36,37] Furthermore, graphene nanosheets tend to stack together because of the strong inter-sheet van der Waals interactions. The stacking of graphene sheets would reduce their porosity, increase the diffusion resistance of reactants/electrolytes, and reduce the number of exposed active sites. Therefore, a careful molecular design of graphene is needed to enable its use as high performance electrocatalysts for practical applications.

Herein, we present the synthesis of three-dimensional (3D) porous nanostructures composed of nitrogen doped holey graphene (NHG) as multifunctional metal-free electrochemical catalysts. The holey surface structure is created on individual graphene sheets to engender more exposed active edge sites. Nitrogen doping further improves the catalytic reactivity, while the formation of 3D porous structures significantly reduces graphene nanosheet stacking and facilitates fast transport of reactants/electrolytes. The three factors work together, leading to superb electrocatalytic activities for both hydrazine oxidation and ORR. Detailed material and electrochemical characterization of NHG was carried out to evaluate its physical structure, chemical composition, electrocatalytic activity and durability.

[a]School of Chemical and Biomedical Engineering, Nanyang Technological University, 62 Nanyang Drive, Singapore 637459. E-mail: chenyuan@ntu.edu.sg; Fax: +65-65156046; Tel: +65-63168939

[b]School of Chemistry and Chemical Engineering, Tianjin University of Technology, Tianjin 300384, P. R. China

[c]Department of Chemical Engineering, Tsinghua University, Beijing 100084, P. R. China

† Electronic supplementary information (ESI) available: AFM images of GO sheets, nitrogen physisorption isotherms, XPS spectrum of RG, RDE curves of electrodes, CV curves of electrodes, and determination of the number of total electrons (n) involved in hydrazine oxidation. See DOI: 10.1039/c3nr34267k

Experimental

Synthesis of NHG sheets

Fig. 1 sketches the three-step synthesis procedure for preparation of NHG and other related materials. First, graphene oxide (GO) was prepared from natural graphite flakes by using a modified Hummers method, and the details were described elsewhere.[38] The as-prepared GO product was readily dispersed in deionized (DI) water to get a stable aqueous solution at a concentration of 1 mg mL^{-1} for use. Then, the in-plane porosity was introduced to the basal plane of GO sheets to form holey GO (HG) sheets using a previously reported procedure with some modifications.[39] Briefly, 5 mL of the above GO aqueous solution (1 mg mL^{-1}) was mixed with 35 mL of concentrated nitric acid (68 wt%) with stirring. The mixture was subsequently subjected to sonication in a bath sonicator (Elmasonic, S 60 H, 500 W) for 15 minutes. After completing sonication, the mixture was settled at room temperature for 2 h and then poured into 150 mL of DI water, centrifuged at 20 000*g*, and washed with DI water several times to remove the acid. The resulting product was dried under vacuum for further use. Lastly, a one-pot hydrothermal process using urea as an abundant low-cost nitrogen source in the presence of HG aqueous solution was used to synthesize NHG, which can achieve simultaneous nitrogen-doping and reduction of HG sheets. In a typical experiment, 10 mL of HG (2 mg mL^{-1}) aqueous dispersion was diluted with 25 mL of DI water, and subsequently 2 g of urea was added into the HG solution with sonication for 1 h. Afterwards, the solution was sealed in a 50 mL Teflon-lined autoclave and maintained at 180 °C for 18 h. The resulting product was filtered and washed with DI water several times. As a control experiment, undoped (without N) reduced GO (RG) and reduced HG (RHG) were also produced under similar one-pot hydrothermal conditions without adding urea into the GO or HG aqueous solution. Prior to electrochemical measurements, the NHG, RG, and RHG samples were treated with a $NaBH_4$ solution (1 M) to further remove the epoxide and hydroxyl functional groups before being transferred onto glassy carbon (GC) electrodes.

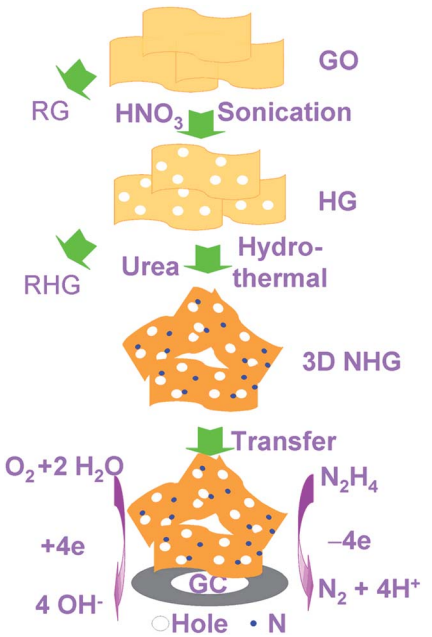

Fig. 1 Schematic illustration of the synthesis of NHG, RG, and RHG sheets by a three-step wet-chemical method.

Materials characterization

The microstructure and morphology of the samples were characterized using a scanning electron microscope (SEM) (Hitachi S-4800) with an acceleration voltage of 5 kV, an atomic force microscope (AFM) (MFP3D, Asylum Research, operating in tapping mode), and a high-resolution transmission electron microscope (HRTEM) (JEOL JEM-2010). Raman spectra of the samples were collected using a Renishaw inVia micro-Raman spectroscopy system with an excitation laser at 514.5 nm. X-ray photoelectron spectroscopy (XPS) analysis was performed on an X-ray photoelectron spectrometer (VG ESCALAB MK II) with an MgKα (1253.6 eV) achromatic X-ray source. Nitrogen physisorption isotherms were measured at 77 K using a Quantachrome Autosorb-6b static volumetric instrument. The samples were first degassed at 250 °C under high vacuum (<0.01 mbar). The specific surface area was calculated by the Brunauer–Emmet–Teller (BET) method.

Electrochemical measurements

Electrochemical measurements of the samples, including NHG, RG, RHG, and Pt–C (10 wt% Pt and 3 wt% Pt), were conducted using a CHI 660D potentiostat. A three-electrode configuration, consisting of a saturated calomel electrode (SCE) as the reference electrode, a platinum wire as the counter electrode, and a GC electrode with the active material deposited on it as the working electrode, was used for the measurements. Rotating disk electrode (RDE) and rotating ring-disk electrode (RRDE) measurements were carried out on a MSRX electrode rotator (Pine Instrument) and the potentiostat. To prepare the working electrode, the active materials were first dispersed in ethanol by sonication. The samples were bath sonicated for 5–15 min to make a relatively homogenous dispersion. The as-prepared dispersion was then immediately drop-cast on a GC electrode, followed by drying in air. The mass loading of all active materials is kept at 0.025 mg per electrode by weighing the material used before and after the casting. At least four electrodes were prepared for each active material by casting them on GC electrodes at the same mass loading to ensure the reproducibility of our results. After that, 10 μL of 0.5 wt% aqueous Nafion solution was further cast over the electrode. The electrode was finally dried in air. The hydrazine oxidation measurements were performed in a 0.1 M phosphate buffer solution (PBS) with pH at 7.4. N_2 was used to purge the solution to achieve the oxygen-free electrolyte solution. The oxygen reduction measurements were carried out in 0.1 M oxygen saturated KOH solution.

Results and discussion

Morphology of NHG

As-prepared GO sheets have a thickness of about 1.4 nm with the lateral size ranging from several hundred nanometers to

several micrometers (see Fig. S1 in ESI†). AFM images in Fig. 2a and b show that the thickness of NHG sheets is around 0.8 nm (the height profile along the Line A). It is smaller than that of GO sheets (1.4 nm), which can be credited to the removal of the surface functional groups from GO surfaces by the hydrothermal treatment. Different from the surface of GO sheets, many dark spots can be observed on NHG sheets (see the inset of Fig. 2a). The height profiles along the Lines B, C, and D in Fig. 2b show that the depth of the dark spots is about 0.7–0.8 nm below the NHG surface. This suggests that the black spots are penetrated pores on the basal plane of graphene. A statistics analysis of AFM images of more than 20 NHG sheets indicates that the pores occupy ~25% of the surface on NHG sheets. The HRTEM image of NHG sheets (Fig. 2d) indicates that the pore size is about 2–5 nm. The size of pores and their surface density increases with the extension of the bath sonication time in HNO_3. Fig. S2 in the ESI† shows that the longer sonication treatment (>1 h) breaks GO sheets into small pieces. In order to obtain a good balance between the density of pores and the electrical transport properties of NHG sheets, the sonication time in HNO_3 was optimized. We found that the optimum sonication time is 15 min. After the hydrothermal treatment, NGH sheets aggregate together forming an interconnected 3D porous bulk material. The photograph in the inset of Fig. 2c shows that the 3D structure can stand alone without collapsing. The SEM image in Fig. 2c indicates that the pore size ranges from a few hundred nanometers to several micrometers. The nitrogen physisorption measurements (Fig. S3 in ESI†) show that the bulk NHG material has a specific surface area of 784 $m^2 g^{-1}$, which is much larger than that of the bulk RG at 277 $m^2 g^{-1}$. Different from conventional stacked graphene films, the 3D porous architectures of NHG with a large surface area and well-defined porosity are expected to render maximum access to the surface of graphene nanosheets, enabling efficient diffusion of reactants/electrolytes, as well as multidimensional electron transport pathways. All these factors are favorable for electrocatalytic reactions.

Physicochemical properties of NHG

XPS was performed to evaluate the chemical composition of NHG sheets. The spectrum of NHG in Fig. 3a has a strong nitrogen peak, indicating that nitrogen species have been successfully incorporated into the graphitic framework. In comparison, XPS spectra of GO (Fig. 3a) and RG (see Fig. S4 in ESI†) do not have nitrogen peaks. No other elements are detected apart from carbon, nitrogen, and oxygen, implying the high purity of samples. XPS elemental quantitative analysis indicates that the NHG has a high nitrogen content of 8.6 at.%. Fig. 3b shows the high-resolution C_{1s} spectra of GO and NHG. The C_{1s} spectrum for NHG shows a considerable decrease of oxygenated carbon related signals in a higher energy region (286–289 eV) after the hydrothermal reaction, confirming the effective recovery of the π-system of graphene.[38] For the C_{1s} spectrum of NHG, the main peak at 284.5 eV is assigned to the C–C bond, indicating that most of the C atoms in NHG are in conjugated honeycomb lattices. Further, the peak located at 285.8 eV is credited to the C–N bond,[40,41] confirming the effective nitrogen doping by the hydrothermal reaction in the presence of urea. The characteristics of N-dopants in NHG sheets are shown by the N_{1s} XPS spectrum in Fig. 3c. The N_{1s} peak can be deconvoluted into three different components at 398.7,

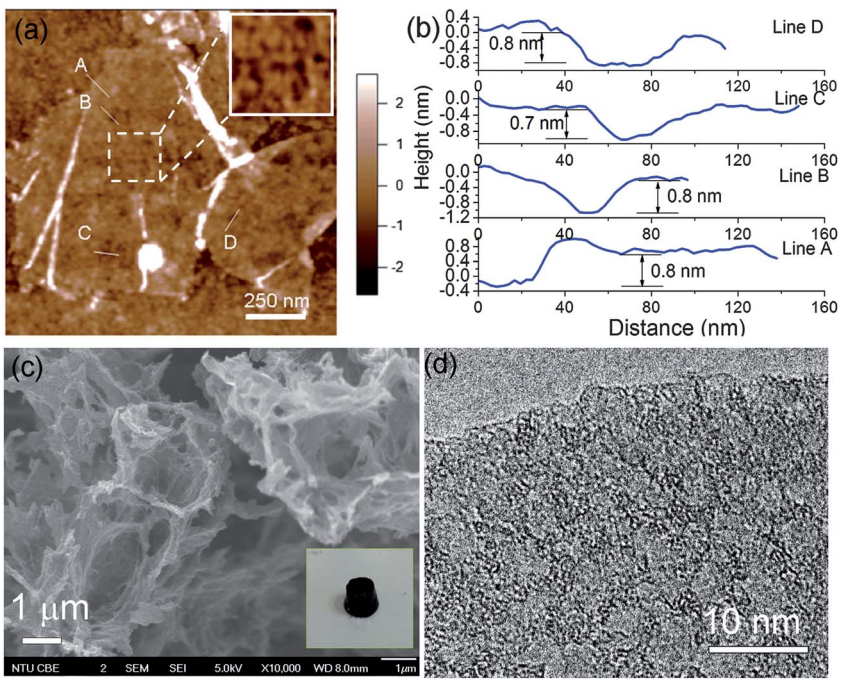

Fig. 2 (a) AFM image of NHG sheets (the inset shows a magnified area with holes), (b) the height profiles along Lines A, B, C, and D in (a), (c) SEM image of NHG with 3D porous structure (the inset shows a photograph of the NHG block), and (d) HRTEM image of NHG sheets.

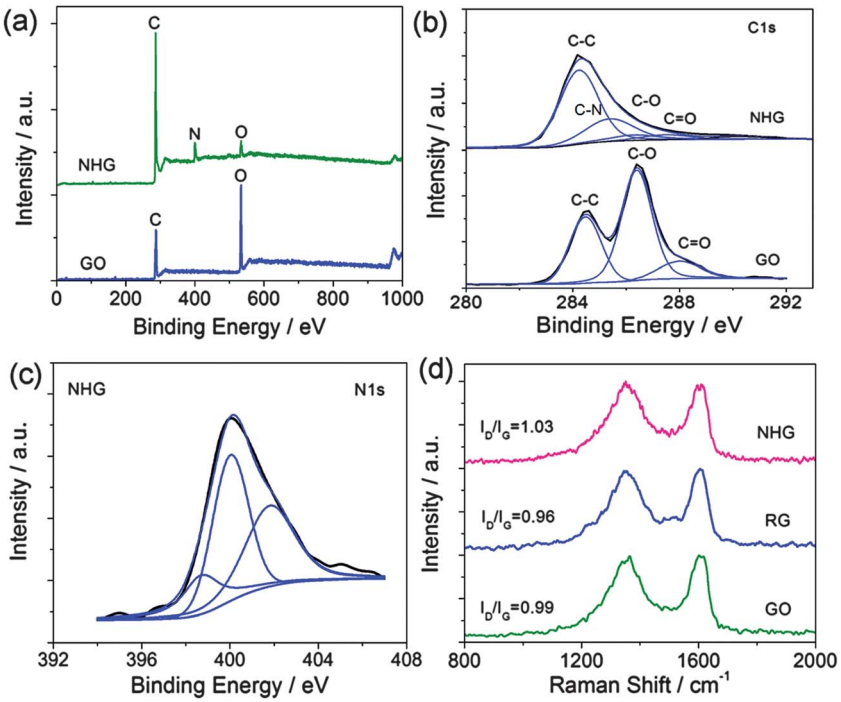

Fig. 3 (a) Survey scans and (b) high resolution C1s spectra of GO and NHG; (c) the high resolution N1s spectrum of NHG; (d) Raman spectra of GO, RG, and NHG.

400.1, and 401.8 eV, which are assigned to pyridinic N, pyrrolic N, and graphitic N, respectively. This agrees with the results obtained from other N-doped carbon nanomaterials.[42]

Raman spectroscopy was also used to characterize NHG, as shown in Fig. 3d. Raman spectra of GO, RG, and NHG have two prominent peaks at 1350 and 1600 cm^{-1}, which correspond to the D band arising from the disordered carbon atoms and the G band from sp^2-hybridized graphitic carbon atoms, respectively. The intensity ratio of the D and G band (I_D/I_G) for graphitic materials is a measure of their structural disorder.[40,43] The I_D/I_G ratio of GO decreased from 0.99 to 0.96, when GO was hydrothermally reduced into RG, suggesting a partial recovery of the π-system.[39] In comparison, the I_D/I_G ratio of NHG ($I_D/I_G = 1.03$) is slightly larger than that of RG ($I_D/I_G = 0.99$), suggesting a broken hexagonal symmetry of graphene, most probably caused by either the heterogeneous N-dopants or the in-plane porosity of graphene.[40,42] Overall, comparing with the commonly used high-temperature (800–1000 °C) methods for preparing nitrogen-doped nanocarbon materials, such as pyrolysis or annealing,[11–13] the hydrothermal method used in this work is effective and sustainable, without harsh experimental conditions, complicated equipment, or toxic gas emission. The nitrogen content up to 8.6 at.% was achieved.

Hydrazine oxidation

Next, we showed that the NHG material with the 3D porous structure is a high performance multifunctional electrocatalyst. First, its excellent activity toward hydrazine oxidation was demonstrated. To the best of our knowledge, this is the first study to exploit the electrooxidation ability of nitrogen doped graphene materials for hydrazine oxidation reactions. Hydrazine is a promising liquid fuel candidate for fuel cells due to its high theoretical electromotive force (1.56 V), high power density, and environmentally benign byproducts.[2] Successful electrocatalytic oxidation of hydrazine, especially without using traditional Pt-based catalysts, is important for the development of direct hydrazine fuel cells. The electrocatalytic performance toward hydrazine oxidation by NHG was evaluated by cyclic voltammetry (CV) measurements. Fig. 4a–e and S5† show CV profiles of different electrodes, including the bare GC, Nafion-coated GC (Nafion/GC), RG/GC, RHG/GC, NHG/GC, and 10 wt% Pt–C/GC in a N_2-saturated 0.1 M PBS (pH = 7.4) with and without 10 mM hydrazine at a scan rate of 20 mV s^{-1}. It should be noted that in order to make a meaningful comparison among different active materials, the mass loading of all active materials on each GC electrode is kept at 0.025 mg. At least four electrodes were prepared for each active material. The peak current densities of electrodes prepared by casting the same amount of RG, HG, NHG, 10 Pt–C% on different GC electrodes are 2.76 ± 0.10, 3.78 ± 0.08, 4.89 ± 0.09, 5.20 ± 0.07 mA cm^{-2}, respectively. The relative error among electrodes prepared by the same material is very small. Both bare GC and Nafion/GC electrodes show poor activity towards hydrazine oxidation without oxidation peaks. In contrast, a large well-defined hydrazine oxidation peak appears at around 0.35 V for the RG/GC, RHG/GC, and NHG/GC electrodes, while no responses were observed for all three electrodes without hydrazine. This suggests that all these graphene-based electrodes catalyze the oxidation of hydrazine. Furthermore, the peak current density of the RHG/GC electrode is much higher than that of the RG/GC electrode, which most probably arises from the presence of more exposed edge sites in RHG.[9] Of the three graphene-based electrodes studied, the NHG/GC electrode is the most active in

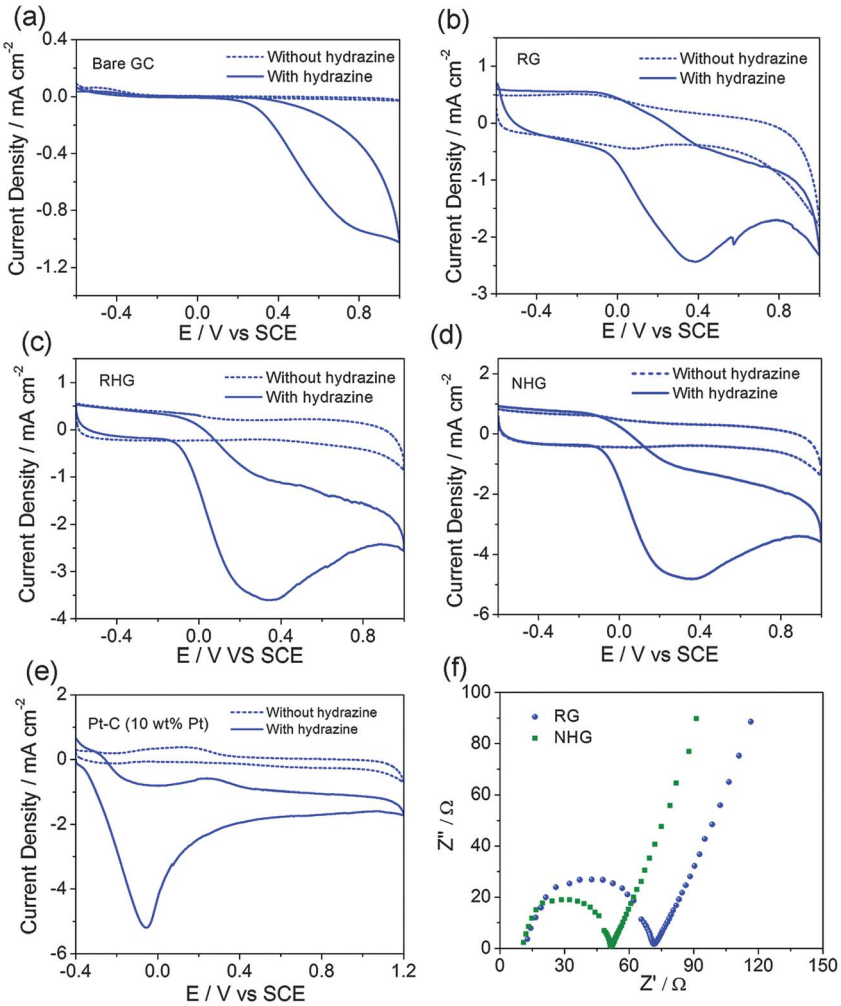

Fig. 4 CV curves obtained on (a) bare GC, (b) RG/GC, (c) RHG/GC, (d) NHG/GC, and (e) 10 wt% Pt–C/GC electrodes in a nitrogen-saturated 0.1 M pH 7.4 PBS solution in the absence (dashed lines) and in the presence (solid lines) of 10 mM hydrazine at a scan rate of 20 mV s^{-1}; (f) Nyquist diagram of RG/GC and NHG/GC electrodes in nitrogen-saturated 0.1 M pH 7.4 PBS solution containing 10 mM hydrazine.

terms of the peak current density, which is comparable to the 10 wt% Pt–C/GC electrode, and much higher than that of the RG/GC electrode at the same concentration of hydrazine. This is most probably a synergetic effect resulting from the enrichment of edge sites and nitrogen dopants, since the presence of heteroatom nitrogen at the carbon surface enhances the electrical conductivity to facilitate charge transport and electrolyte–electrode interaction.[9] The substantial increase in the peak current density for the NHG/GC electrode reflects a faster electron-transfer for hydrazine oxidation than RG/GC, which is further supported by electrochemical impedance spectra. Fig. 4f shows the Nyquist diagram of the RG/GC and NHG/GC electrodes in 0.1 M PBS solution containing 10 mM hydrazine. The charge-transfer resistance corresponding to the semicircle diameter[15] in the Nyquist impedance plot is 40 Ω for the NHG/GC electrode and 60 Ω for the RG/GC electrode. This confirms that electrons for hydrazine oxidation can be transferred much easier by NHG relative to RG.

To further investigate the electrocatalytic activity for hydrazine oxidation of NHG, both CV and RDE measurements were carried out using different electrodes in 0.1 M PBS solution (pH = 7.4) as a function of hydrazine concentration (see Fig. 5 and S6–S9 in the ESI†). Fig. 5a shows that the catalytic oxidation current density of the NHG/GC electrode increases with the increase of hydrazine concentration, while the oxidation peak position has a positive shift. Moreover, the electrochemical response is irreversible as no current is observed during the reverse sweep. RDE measurements (Fig. 5b) show that the onset potential for hydrazine oxidation on the NHG/GC electrode is as low as −0.15 V *vs.* SCE. The mass activity at constant potential (0.3 V) as a function of hydrazine concentration obtained from RDE measurements of different electrodes (RG/GC, RHG/GC, NHG/GC, 3 wt% Pt–C/GC, and 10 wt% Pt–C/GC) is plotted together in Fig. 5c. The NHG/GC electrode affords a high mass activity of about 78 mA mg^{-1} at 0.3 V in the presence of 50 mM hydrazine, which is much higher than that of the RG/GC, RHG/GC, and 3 wt% Pt–C/GC electrodes. The catalytic performance of the NHG/GC electrode is also much superior to other reported carbon-based metal-free electrocatalysts under similar conditions in terms of both onset potential and mass activity.[9,33]

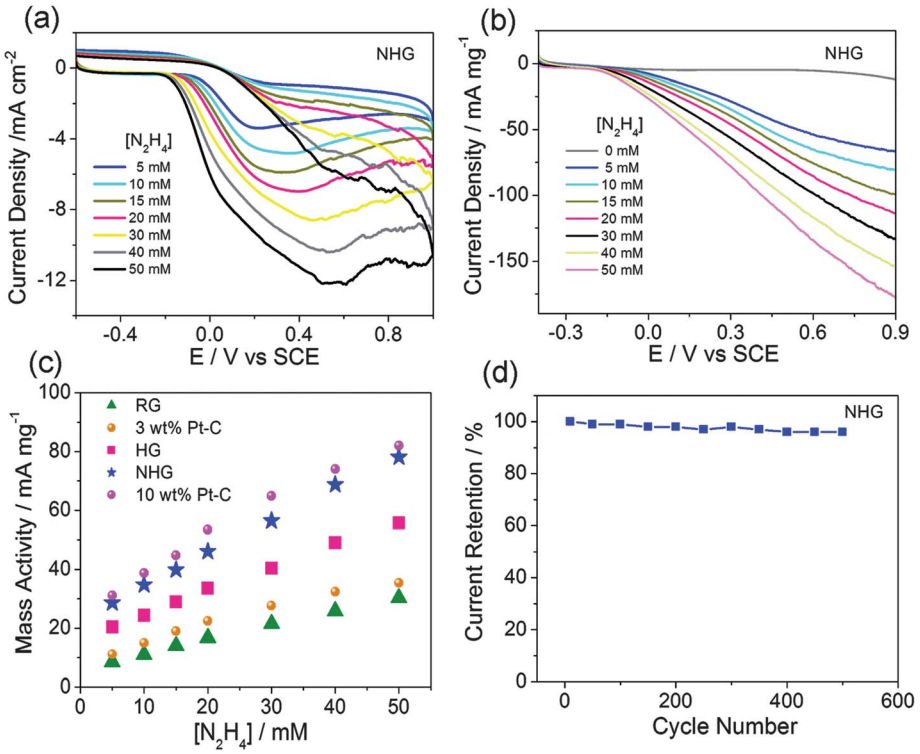

Fig. 5 (a) CV curves at 20 mV s^{-1} of a NHG/GC electrode in 0.1 M PBS solution (pH = 7.4) as a function of hydrazine concentration, (b) RDE curves at 20 mV s^{-1} of the NHG/GC electrode at a rotation rate of 900 rpm as a function of hydrazine concentration; (c) mass activity at a constant potential (0.3 V) as a function of hydrazine concentration of the RG/GC, RHG/GC, NHG/GC, 3 wt% Pt–C/GC, and 10 wt% Pt–C/GC electrodes obtained from RDE curves; (d) the retention of peak current density of hydrazine oxidation in successive detections of 10 mM hydrazine at the NHG/GC electrode as a function of cycle number.

Although the onset potential of the NHG is still higher than the commercial 10 wt% Pt–C/GC electrodes, the current generation ability (normalized by the loading mass) at the same potential is comparable to that of the commercial 10 wt% Pt–C/GC electrodes. Furthermore, the number of total electrons (n) involved in hydrazine oxidation can be determined to be about 3.9, according to the following equation:[44] $I_p = 3.01 \times 10^5 n[(1-\alpha)n_\alpha]^{1/2} A C_h D^{1/2} \nu^{1/2}$, where I_p, n, α, A, C_h, and D are peak current, electron transfer number, electron transfer coefficient, electrode surface area, hydrazine concentration, and hydrazine diffusion efficient, respectively (see Fig. S10–S13†). We propose that the overall reaction of the hydrazine oxidation catalyzed by NHG is as follows:[45,46] $N_2H_4 \rightarrow N_2 + 4H^+ + 4e^-$. Lastly, catalyst durability is important for the long-term operation of fuel cells. As shown in Fig. 5d, the NHG shows excellent durability for hydrazine oxidation, with only 4% loss of the initial steady state peak current density after 500 cycles, indicating a great potential for direct liquid fuel cell applications.

Oxygen reduction

Next, we showed that the NHG also has excellent electrocatalytic activity for ORR. The development of Pt/C alternatives as ORR electrocatalysts is a major trend in fuel cell research.[10,47] One previous report has reported that CVD grown N-doped graphene[24] has excellent ORR activity. However, its performance is still restricted by poor mass transfer due to the stacking of graphene sheets. We expected that the porous 3D nanostructure composed of holey graphene sheets developed in this work would facilitate the rapid transport of reactants/electrolytes. The RDE experiments were used to characterize the ORR activity of various electrodes, including RG/GC, RHG/GC, NHG/GC, and 20 wt% Pt–C/GC, in an aqueous solution of O_2-saturated, 0.1 M KOH at a rotation rate of 1600 rpm and a scan rate of 10 mV s^{-1}. Fig. 6a shows that the HG/GC electrode has much higher limiting current density with more positive onset potential than that of the RG/GC electrode, indicating that the active edge-plane sites can enhance the ORR activity. The onset potential of the NHG/GC electrode for ORR is at −0.08 V, which is more positive than those of the HG/GC (−0.16 V) and RG/GC (−0.22 V) electrodes, as well as the previously reported CVD grown nitrogen-doped graphene (−0.2 V).[24] Moreover, the limiting current density of the NHG/GC electrode is also much higher than those of the HG/GC and RG/GC electrodes. These results show that the NHG/GC electrode has better electrocatalytic activity for ORR than other graphene based electrodes studied in the present work. We attributed the enhanced ORR activity of NHG to the synergic effect of nitrogen dopants and edge sites. To our surprise, although the onset potential for the NHG/GC electrode was still slightly more negative than that of the 20 wt% Pt–C/GC electrode (−0.01 V), it has a much stronger limiting current than the Pt–C/GC electrode. The corresponding electron-transfer numbers per oxygen molecule for ORR at the NHG/GC electrode is 3.85 at the potential of −0.4 V according to

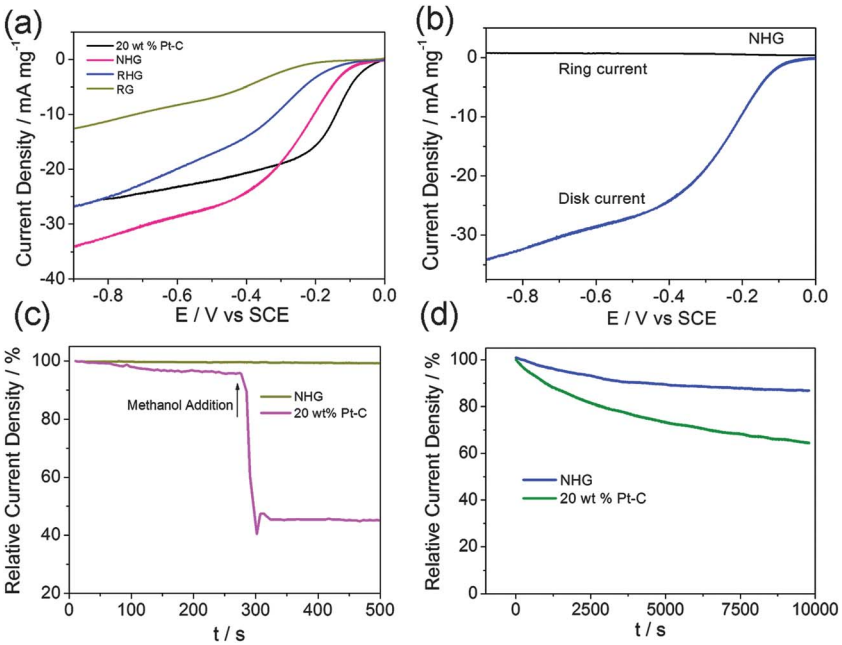

Fig. 6 (a) RDE voltammograms of the RG/GC, RHG/GC, NHG/GC, and 20 wt% Pt–C/GC electrodes in an O_2-saturated, 0.10 M KOH solution at a rotation rate of 1600 rpm. Scan rate: 10 mV s^{-1}; (b) RRDE voltammogram of the NHG/GC electrode in an O_2-saturated, 0.1 M KOH aqueous solution at a scan rate of 10 mV s^{-1} at 1600 rpm; (c) current–time (*j*–*t*) chronoamperometric response for ORR at the NHG/GC electrode and the 20 wt% Pt–C/GC electrode upon introduction of 1 M methanol after about 300 s at −0.25 V; (d) chronoamperometric response of the NHG/GC electrode and the 20 wt% Pt–C/GC electrode at −0.25 V in an O_2-saturated 0.10 M KOH aqueous solution.

the RRDE measurements in Fig. 6b,[11] suggesting that it is an efficient four-electron transfer pathway. All these results show that NHG is a promising electrocatalyst for ORR in an alkaline solution with highly competitive performance at a much lower cost than the benchmarked Pt/C catalysts.

For practical applications of ORR, the resistance to the methanol crossover and the durability are important issues for evaluating electrocatalysts. The chronoamperometric response of the 20 wt% Pt–C/GC electrode has a sharp decrease in the current when 1 M methanol is added (Fig. 6c). In contrast, the amperometric response of the NHG/GC electrode remains nearly unchanged after the addition of methanol, suggesting a better methanol tolerance. Continuous oxygen reduction (*ca.* 10 000 s) at −0.25 V (*vs.* SCE) on the NHG/GC electrode results in a 10% loss in current density before leveling off (Fig. 6d), as compared to the 36% loss of the Pt/C electrode under the same testing conditions. These results suggest that active sites on the NHG/GC electrode are more stable than those on the commercial Pt/C electrode. The NHG can be a promising electrocatalyst for direct methanol and alkaline fuel cells.

Conclusions

A 3D porous nanostructure composed of nitrogen-doped holey graphene sheets was synthesized. The resulting material possesses a high nitrogen content of up to 8.6 at.% and a large specific area of ~784 m^2 g^{-1}, and shows a remarkable electrocatalytic activity for both hydrazine oxidation and oxygen reduction with excellent durability. Its electrochemical catalytic activities toward both reactions are much better than those of reduced graphene oxides. Some performance characteristics of electrodes fabricated using NHG, such as the current generation, the limiting current, and the resistance to the methanol crossover, are comparable or even better than commercial 10 to 20 wt% Pt–C catalysts. The outstanding electrocatalytic activity can be credited to its abundant edge sites, high-level nitrogen doping, and 3D porous nanostructure. Our work demonstrates the importance of molecular design of graphene based materials as high performance metal-free electrochemical catalysts. We expect that the new NHG material and its synthesis approach can open new avenues for the development of commercially feasible metal free catalysts for broad applications.

Acknowledgements

This work was supported by National Research Foundation, Singapore (Grants: NRF-CRP2-2007-02) and Ministry of Education, Singapore (MOE2011-T2-2-062).

References

1 M. Armand and J. M. Tarascon, *Nature*, 2008, **451**, 652–657.
2 A. Serov and C. Kwak, *Appl. Catal., B*, 2010, **98**, 1–9.
3 B. Lim, M. Jiang, P. H. C. Camargo, E. C. Cho, J. Tao, X. Lu, Y. Zhu and Y. Xia, *Science*, 2009, **324**, 1302–1305.
4 L. Q. Ye, Z. P. Li, H. Y. Qin, J. K. Zhu and B. H. Liu, *J. Power Sources*, 2011, **196**, 956–961.

5 J. Sanabria-Chinchilla, K. Asazawa, T. Sakamoto, K. Yamada, H. Tanaka and P. Strasser, *J. Am. Chem. Soc.*, 2011, **133**, 5425–5431.
6 F. Jia, J. Zhao and X. Yu, *J. Power Sources*, 2013, **222**, 135–139.
7 H. Yang, X. Zhong, Z. Dong, J. Wang, J. Jin and J. Ma, *RSC Adv.*, 2012, **2**, 5038–5040.
8 U. Martinez, K. Asazawa, B. Halevi, A. Falase, B. Kiefer, A. Serov, M. Padilla, T. Olson, A. Datye, H. Tanak and P. Atanassov, *Phys. Chem. Chem. Phys.*, 2012, **14**, 5512–5517.
9 R. Silva, J. Al-Sharab and T. Asefa, *Angew. Chem., Int. Ed.*, 2012, **51**, 7171–7175.
10 D. Yu, E. Nagelli, F. Du and L. Dai, *J. Phys. Chem. Lett.*, 2010, **1**, 2165–2173.
11 K. P. Gong, F. Du, Z. H. Xia, M. Durstock and L. M. Dai, *Science*, 2009, **323**, 760–764.
12 R. Liu, D. Wu, X. Feng and K. Müllen, *Angew. Chem., Int. Ed.*, 2010, **49**, 2565–2569.
13 S. Chen, J. Bi, Y. Zhao, L. Yang, C. Zhang, Y. Ma, Q. Wu, X. Wang and Z. Hu, *Adv. Mater.*, 2012, **24**, 5593–5597.
14 X. Xu, S. J. Jiang, Z. Hu and S. Q. Liu, *ACS Nano*, 2010, **4**, 4292–4298.
15 X. Xu, L. Yang, S. Jiang, Z. Hu and S. Liu, *Chem. Commun.*, 2011, **47**, 7137–7139.
16 M. Q. Zhao, Q. Zhang, J. Q. Huang and F. Wei, *Adv. Funct. Mater.*, 2012, **22**, 675–694.
17 H. Wang, B. Wang, X. Y. Quek, L. Wei, J. W. Zhao, L. J. Li, M. B. Chan-Park, Y. H. Yang and Y. Chen, *J. Am. Chem. Soc.*, 2010, **132**, 16747–16749.
18 C. M. Chen, Q. Zhang, X. Zhao, B. Zhang, Q. Kong, M. Yang, Q. Yang, M. Wang, Y. Yang, R. Schlogl and D. Su, *J. Mater. Chem.*, 2012, **22**, 14076–14084.
19 D. Yu, Q. Zhang and L. Dai, *J. Am. Chem. Soc.*, 2010, **132**, 15127–15129.
20 X. C. Wang, K. Maeda, A. Thomas, K. Takanabe, G. Xin, J. M. Carlsson, K. Domen and M. Antonietti, *Nat. Mater.*, 2009, **8**, 76–80.
21 M. Zhong, E. K. Kim, J. P. McGann, S.-E. Chun, J. F. Whitacre, M. Jaroniec, K. Matyjaszewski and T. Kowalewski, *J. Am. Chem. Soc.*, 2012, **134**, 14846–14857.
22 Y. Li, Y. Zhao, H. Cheng, Y. Hu, G. Q. Shi, L. M. Dai and L. T. Qu, *J. Am. Chem. Soc.*, 2012, **134**, 15–18.
23 J. Liang, Y. Zheng, J. Chen, J. Liu, D. Hulicoa-Jurcakova, M. Jaroniec and S. Qiao, *Angew. Chem., Int. Ed.*, 2012, **51**, 3892–3896.
24 L. Qu, Y. Liu, J. B. Baek and L. Dai, *ACS Nano*, 2010, **4**, 1321–1326.
25 E. Y. Wang, Y. Wan and D. Zhang, *Electrochem. Commun.*, 2010, **12**, 187–190.
26 C. Huang, C. Li and G. Shi, *Energy Environ. Sci.*, 2012, **5**, 8848–8868.
27 D. Yu, E. Nagelli, R. Naik and L. Dai, *Angew. Chem., Int. Ed.*, 2011, **50**, 6575–6578.
28 D. Yu, Y. Yang, M. Durstock and L. Dai, *ACS Nano*, 2010, **4**, 5633–5640.
29 X. W. Yang, J. W. Zhu, L. Qiu and D. Li, *Adv. Mater.*, 2011, **23**, 2833–2838.
30 Y. Zhu, S. Murali, W. Cai, X. Li, J. W. Suk, J. R. Potts and R. S. Ruoff, *Adv. Mater.*, 2010, **22**, 3906–3924.
31 H. Bai, C. Li and G. Shi, *Adv. Mater.*, 2011, **23**, 1089–1115.
32 Y. Li, W. Zhou, H. Wang, L. Xie, Y. Liang, F. Wei, J. Idrobo, S. J. Pennycook and H. Dai, *Nat. Nanotechnol.*, 2012, **7**, 394–400.
33 M. Hadi, A. Rouhollahi and M. Yousefi, *Sens. Actuators, B*, 2011, **160**, 121–130.
34 A. Ambrosi, A. Bonanni and M. Pumera, *Nanoscale*, 2011, **3**, 2256–2260.
35 C. E. Banks, T. J. Davies, G. G. Wildgoose and R. G. Compton, *Chem. Commun.*, 2005, 829–841.
36 E. P. Randviir and C. E. Banks, *RSC Adv.*, 2012, **2**, 5800–5805.
37 D. A. C. Brownson, C. W. Foster and C. E. Banks, *Analyst*, 2012, **137**, 1815–1823.
38 S. B. Liu, T. Y. Zeng, M. Hofmann, E. Burcombe, J. Wei, R. R. Jiang, J. Kong and Y. Chen, *ACS Nano*, 2011, **5**, 6971–6980.
39 X. Zhao, C. M. Hayner, M. C. Kung and H. H. Kung, *ACS Nano*, 2011, **5**, 8739–8749.
40 Y. Zhang, K. Fugane, T. Mori, L. Niu and J. Ye, *J. Mater. Chem.*, 2012, **22**, 6575–6580.
41 D. Yu, Y. Xue and L. Dai, *J. Phys. Chem. Lett.*, 2012, **3**, 2863–2870.
42 D. Deng, X. Pan, L. Yu, Y. Cui, Y. Jiang, J. Qi, W. X. Li, Q. Fu, X. Ma, Q. Xue, G. Sun and X. Bao, *Chem. Mater.*, 2011, **23**, 1188–1193.
43 Y. Zhou, Q. Bao, L. Ai, L. Tang, Y. Zhong and K. P. Loh, *Chem. Mater.*, 2009, **21**, 2950–2956.
44 J. Li and X. Q. Lin, *Sens. Actuators, B*, 2007, **126**, 527–535.
45 M. M. Ardakani, P. E. Karami, P. Rahimi, H. R. Zare and H. Naeimi, *Electrochim. Acta*, 2007, **52**, 6118–6124.
46 B. Dong, B. He, J. Huang, G. Gao, Z. Yang and H. Li, *J. Power Sources*, 2008, **175**, 266–271.
47 Y. Zheng, Y. Jiao, M. Jaroniec, Y. Jin and S. Z. Qiao, *Small*, 2012, **8**, 3550–3566.

